International Forum on Aeroelasticity and Structural Dynamics
IFASD 2024
17-21 June 2024, The Hague, The Netherlands

EXPERIMENTAL INVESTIGATION OF SHOCK CONTROL BUMBS ON THE TRANSONIC DIP OF THE OAT15A AIRFOIL

A. Altkuckatz*, M. Braune, J. Dillinger, M. M. Müller, T. Büte, C. Hanke, H. Ernst, H. Böhlken, P. Hartl, T. Schmidt, H. Mai

German Aerospace Center (DLR),
Institute of Aeroelasticity
Bunsenstraße 10, 37073 Göttingen, Germany
Anna.Altkuckatz@dlr.de

Keywords: Transonic Dip, Shock Control Bumps (SCBs), Flatter, LCO

Abstract: Research on Shock Control Bumps (SCBs) for aeroelastic stability at transonic velocities is growing in importance. A wind tunnel flutter test was conducted at the Transonic Wind Tunnel Göttingen (TWG) using an OAT15A airfoil with a one-meter wingspan and 0.3 m chord. Aeroelastic behavior was tested at Mach numbers from 0.5 to 0.83 and pressures of 30 to 100 kPa. The first test evaluated the "clean profile" and three bump configurations at 50% chord, varying in height. Results showed a reduced transonic dip, and a change in flutter behavior from heave-dominated to pitch-dominated oscillations. A second test aims to resolve the three-dimensional pressure distribution using unsteady pressure-sensitive paint (iPSP) for detailed aerodynamic assessment, including shock dynamics.

The paper will elaborate on the test setups and observed aerodynamic and aeroelastic effects on the OAT15A airfoil, discussing the relationship between SCB aerodynamics and resulting aeroelastic behavior.

1 INTRODUCTION

The flutter phenomenon is a self-induced oscillation that can occur when a flexible structure interacts with an airflow. Flutter can lead to large-amplitude vibrations that may cause structural damage or failure. Therefore, it is crucial to predict and prevent flutter in the design of aircraft wings, wind turbines, bridges, and other structures exposed to aerodynamic loads.

Transonic flutter is particularly challenging, as it involves complex shock wave interactions that affect the pressure distribution and the unsteady aerodynamic forces on the structure.

One possible way to mitigate transonic flutter is to use shock control bumps (SCBs), which are small protuberances on the airfoil surface that modify the shock location and strength. SCBs have been shown to improve the aerodynamic efficiency, to enhance off-design performance by delaying buffet and increasing the drag-divergence Mach number [1], and lift-to-drag ratio of airfoils and wings by reducing the wave drag reduction on laminar-flow airfoils [2]. Moreover, SCBs can also influence the aeroelastic stability [3], [4], [5].

However, there are many concepts for the structural and aerodynamic design of SCBs [6], [7], [8], [9] but the design and optimization of SCBs for aeroelastic purposes is still not straightforward, as it depends on many factors, such as the bump shape, size, location, number, and arrangement, as well as the Mach number, Reynolds number, angle of attack, and structural properties of the airfoil. Therefore, more experimental and numerical investigations are needed to understand the underlying physics of SCBs and their impact on transonic flutter.

In this paper, are the results of a wind tunnel experiment conducted at the Transonic Wind Tunnel Göttingen (TWG) using the OAT15A [10], [11], [12] airfoil model equipped with different SCB configurations presented. The main objectives of the experiment were:

- To measure the flutter boundary and the flutter mode shape of the clean and bumped airfoil at various Mach numbers and pressures.
- To evaluate the effectiveness of SCBs for increasing the flutter speed and altering the flutter characteristics of the airfoil.

The paper is organized as follows: Section 2 describes the model design and the experimental setup, including the identification of the critical load cases. Section 3 presents and discusses the main findings of the flutter. Section 4 summarizes the conclusions and provides some recommendations for future work.

2 MODEL DESIGN AND EXPERIMENTAL SETUP

2.1 Model Design

The model design aims to create a wing that is representative of a typical transonic civil aircraft, but with simplified geometry and structural properties. The wing has a supercritical cross-section and no sweep, which reduces the complexity of the aerodynamic analysis and the manufacturing process. The wing is also assumed to be rigid and has no control surfaces or mass balancers. The main parameters of the wing are shown in Table 1.

Parameter	Value
Span, b (m)	0.997
Chord, c (m)	0.3
Profil	OAT15A
Elastic axis, e (m)	0.075 (c/4)
Thickness reserve, x_D (m)	0.0982
Max. profil thickness, D (m)	0.0368571

Table 1: Model parameters

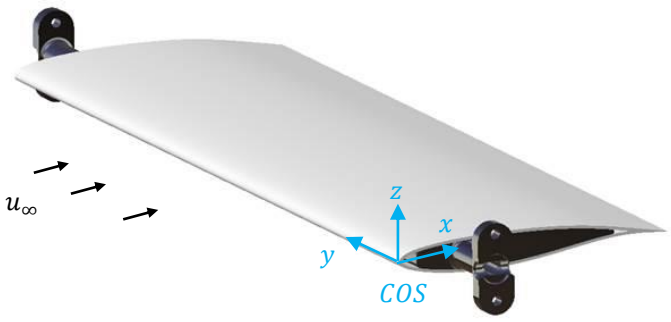

Figure 1: OAT15A Model

For the profile, the well-known OAT15A profile with a trailing edge of 1 mm is used. The model itself is built from two half-shells, three rectangular ribs, and eight spars. Figure 1 shows the model and its coordinate system (COS).

2.1.1 Identification of Critical Load Cases

The measurements are conducted statically and dynamically at a reduced channel pressure of $p_0 \in [50; 60; 70; 80; 90]\ kPa$ and $T_0 = 303.15\ K$. A total of 1713 load cases from the CFD investigations were considered, where the angle of attack varied between $-4°$ and $6°$. The DLR-TAU code was used as the solver with the $k-\omega$ (EARSM) turbulence model.

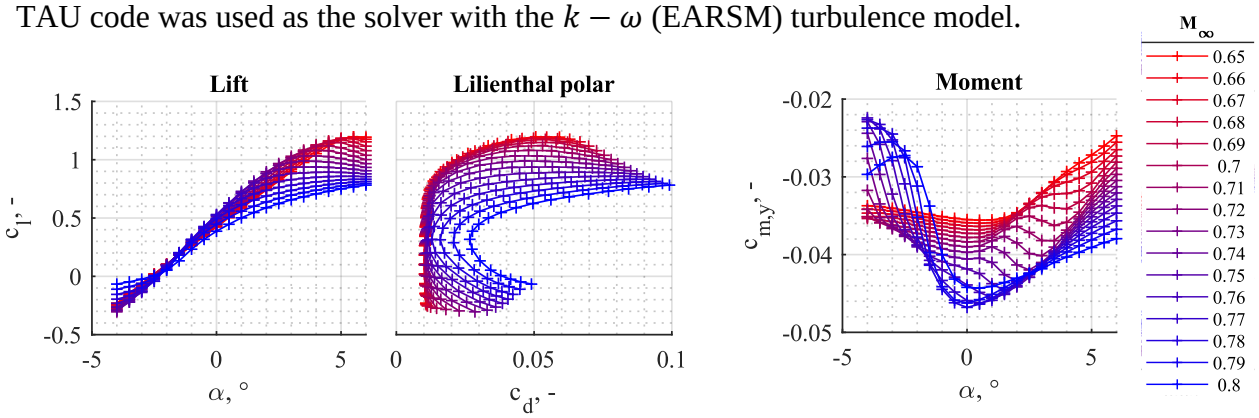

Figure 2 Aerodynamic coefficients at $p_0 = 90\ kPa$

For the dynamic measurements, the load vectors from the CFD investigation were multiplied by a factor of 1.3. Assuming a conservative load distribution, the forces and moments were distributed onto the model using Föpple, allowing the bearing reactions to be ultimately determined. With Föpple, the bearing reaction for all load cases from the CFD was determined, thereby identifying the critical load cases.

2.1.2 Finite Element Modeling and Calculation

The finite element design of the wing (excluding the aluminum root ribs) was carried out using MSC-Nastran for the load cases listed in Table 2.

	p_0 Pa	Ma_∞	α_0 °	c_l	c_d	c_m	φ_∞ kg/m^3	v_∞ m/s	q_∞ Pa
L1	90000	0.68	5.0	1.17	0.05	-0.03	0.83	227.2	21398
L2	90000	0.8	6.0	0.78	0.10	-0.04	0.77	263.1	26476
L3	90000	0.79	0.0	0.45	0.02	-0.05	0.77	260.1	26075
L4	90000	0.65	6,0	1.19	0.06	-0.02	0.84	218.0	20061

Table 2: Critical Load Cases; c_m relates to c/4

Figure 3 (left) shows the maximum expected model deformations for the load cases for the static scenario. It can be seen that the model experiences a maximum deflection of approximately $0.32\ mm$ at the midpoint of the wing span for load case L1, and a maximum torsion of approximately $0.03\ deg$ for load case L4, also at the midpoint of the wing span.

The layers were evaluated for failure by examining the load cases listed in Table 2, considering a dynamic safety factor of 1.3. The failure criterion of each individual layer for load case L1 was considered. The maximum failure index for both cases is approximately 0.1. An index <1 rules out failure of the fiber, while an index >1 indicates an expected failure/breakage of the fiber. Therefore, failure/breakage of the fiber is unlikely. The safety factor is thus $\nu = 9.8 > \nu_{crit} = 4\nu = 9.8 >$

$\nu_{crit} = 4$. Figure 3 (right) shows the first three eigenmodes of the wing. The first bending eigenmode is approximately 347 Hz.

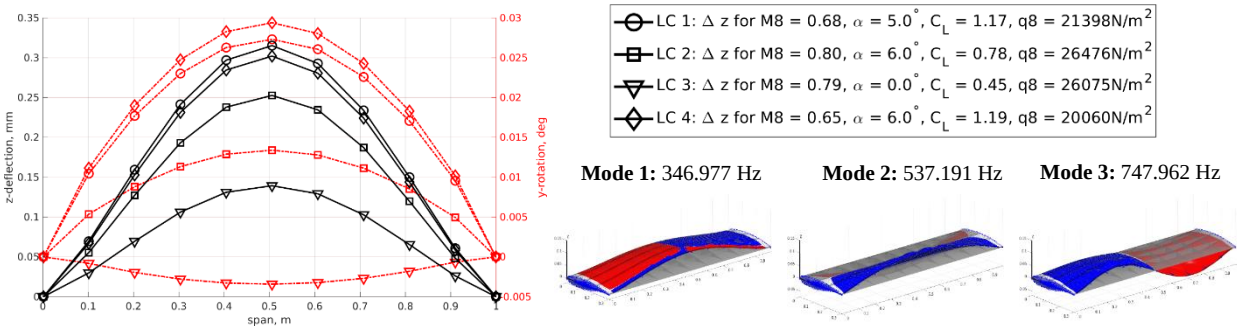

Figure 3: Wing deformation and rotation from FE (left); Eigenmodes (right)

The calculation of the von Mises stresses occurring in the root rib was carried out using Catia - Generative Structural Analysis. A "Distributed Load" was assumed as the load, along with a moment with a point of action on the c/4 line, at the midpoint of the wing span. The calculations were performed for all load cases listed in Table 2, with load case L1 being the case where the highest von Mises stresses occurred.

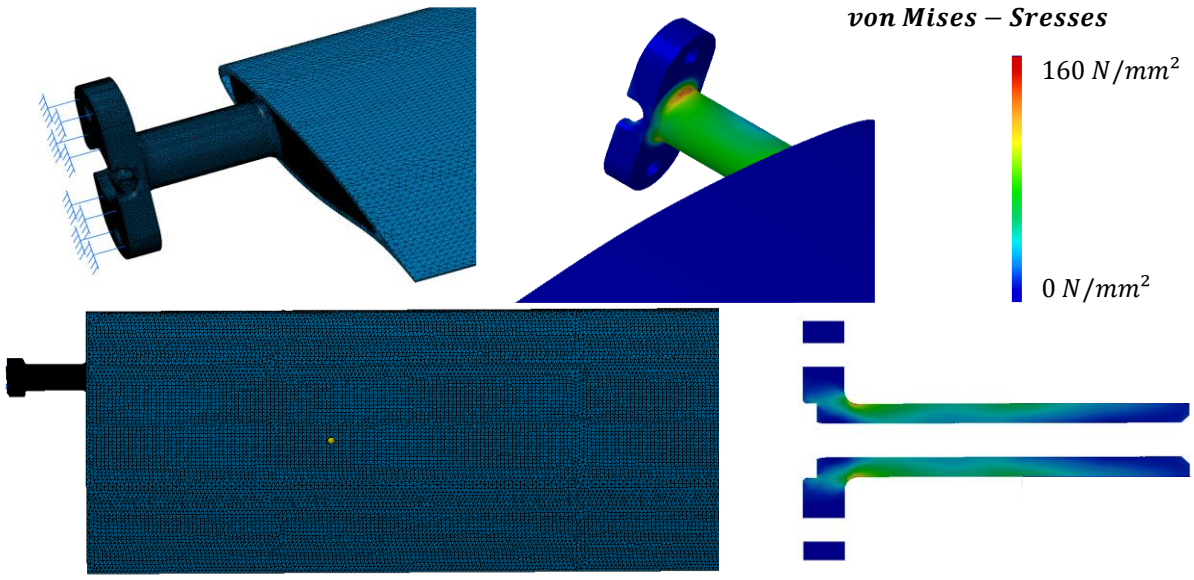

Figure 4: FEM mesh generated with CATIA v5 (left); von Mises-Stresses (right)

The finite element modeling (FEM) (see Figure 4) includes the wing skin, the ribs, as well as the root ribs. The wing spars were neglected. Additionally, for the FEM modeling, the connections between the spars and the wing skin, as well as between the spars and the root ribs, were assumed to be rigid. The maximum von Mises reference stress in the root ribs is 160 N/mm².

2.1.3 Building the wing with load carrying wing skins and a foam core to support the skins and prevent buckling

The wing is composed of load bearing wing skins, which are divided into upper and lower parts that are laminated in different molds and joined with three shear webs and the aluminum root ribs. The shear webs are located at 20%, 45%, and 70% relative chord position and are constructed as a sandwich with a 3 mm foam core (Rohacell with a density of 120 kg/m^3) and a 20-layer glass fabric with $160g/m^2$ on both sides of the core material. The shear webs protrude 30 mm on both sides into the root ribs. The root ribs extend 60 mm into the wing. The load-carrying skins are made from a UD fabric 'Dialead K63716' with an areal weight of $250g/m^2$. The symmetrical structure consisting of twelve individual layers with different layer angles is shown in Figure 5

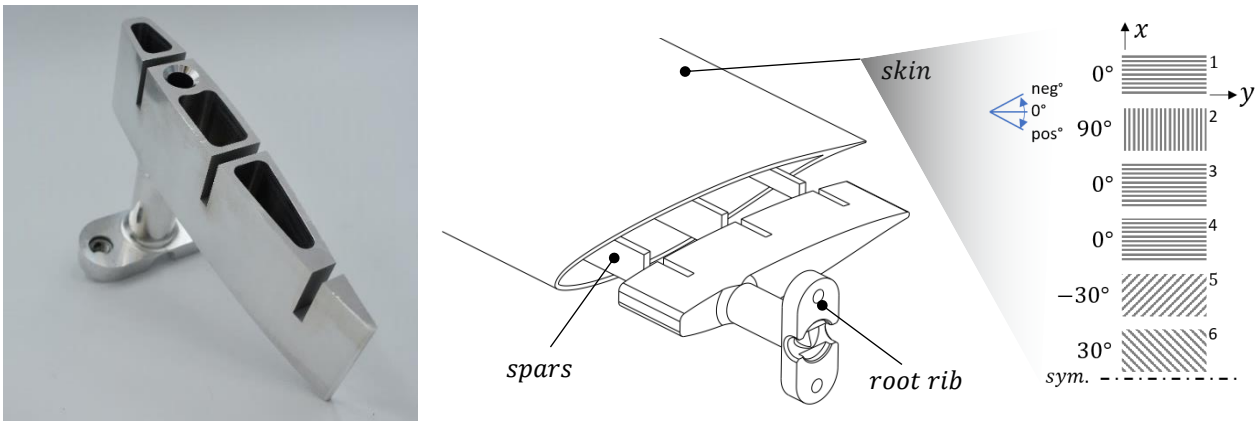

Figure 5: Root rib (left), Composite (center), Fabric (right)

(right). To achieve a smooth surface, an outer finishing layer made of a lightweight glass fabric ($49g/m^2$) is applied. The wings are fastened by means of root ribs, which are glued in on both sides. The root ribs were constructed from high-strength aluminum EN-AW-7022. For the fastening, Ensat threaded inserts were used. Figure 5 (left) shows the final root rib.

2.2 Experimental Setup

The experiments took place in the Transonic Wind Tunnel Göttingen (TWG), which is a closed circuit windtunnel, allowing continuous operation with variable densities at sub-, trans- and supersonic speeds. There are three exchangeable test sections which can be used. For this experiment the “Adaptive Test Section” and the 2D flutter Test Support (see Figure 6) were used. The Adaptive Measurement Section can change its walls to mimic freestream conditions, which enables high Mach number investigations, the flutter test stand allows free pitch and heave motion of the model. The angle of attack α and the heave h were measured by different laser triangulators (h), shown in Figure 6. α is defined as:

$$\alpha = \alpha_{unst} + \alpha_{2D},$$

where α_{unst} is the “un-steady” measured torsion and α_{2D} is the “steady” angle of the 2D- Support (i). The heave h is defined as the distance between the chord line in the neutral position and the current chord line. Two four-element piezoelectric balances (b) (one on each side) measured lift, drag and pitching moment. The test section had a 1.0 x 1.0 m² cross-section and Mach numbers from 0.5 to 0.78 with pressures between 30 kPa and 100 kPa. The wing was linked to a beam (f) with masses to adjust the model's frequency and inertia. The beam connected to the Torsional

spring (c), the piezoelectric balances (b) and the Leaf spring. The springs adjusted the flutter-frequencies.
The wind tunnel model is equipped with 16 unsteady pressure sensors (Kulite). The Kulites are located at the midpoint of the span, distributed over the chord. In the area of the shock movements, there is a higher sensor density to make a more accurate statement about the shock position.

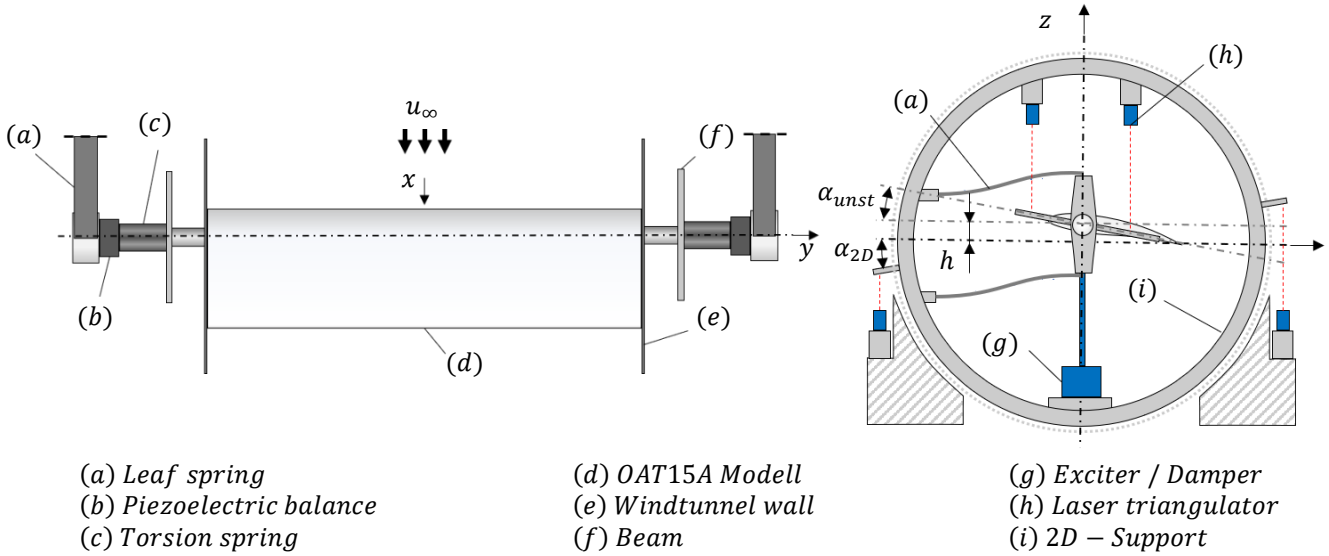

Figure 6: Schematic of the experimental test setup used in the TWG, Figure modified after [13]

Additionally, ten unidirectional acceleration sensors (PCBs) are integrated (orientated in z-direction). Five of these are applied at the leading edge and five more at the trailing edge. Furthermore, four temperature sensors (NiCr-Ni) are integrated into the model. The sensor positions can be found in Figure 7. In addition to the sensors integrated into the model an infrared camera is used the measure the temperature on the model upper side.

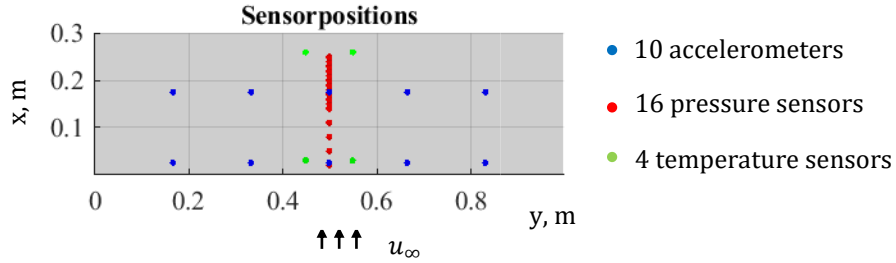

Figure 7: Model integrated sensor positions

2.2.1 Bump and Configurations

For the investigation of the influence of bumps on the transonic dip, three bump configurations were chosen. The contour of the bump was selected in such a way that it can still be manufactured

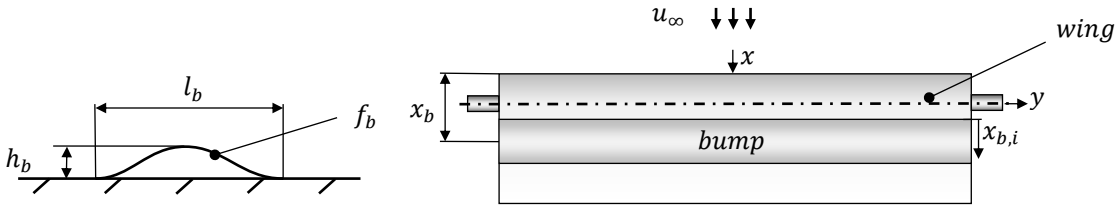

Figure 8: Bump

with reasonable effort and can also be easily implemented later during integration into the wing. Furthermore, the shape of the bump can be realized relatively easily through suitable actuators or through morphing.

This led to the choice of one of the functions of the bump as:

$$f_b = -h_b/2 * cos(2\pi * x_{b,i} * l_b)$$

where f_b is the function of the bump, h_b is the height of the bump, and l_b is the length of the bump.

The position of the bump was chosen so that the highest position of the bump for various Mach numbers lies on or just before the shock positions, at $x_b = 50\%$ of the chord. The bump itself extends over the entire span of the wing and has a length of $l_b = 20\%$ of the chord.

For the first study, the parameters of the height of the bump were varied.

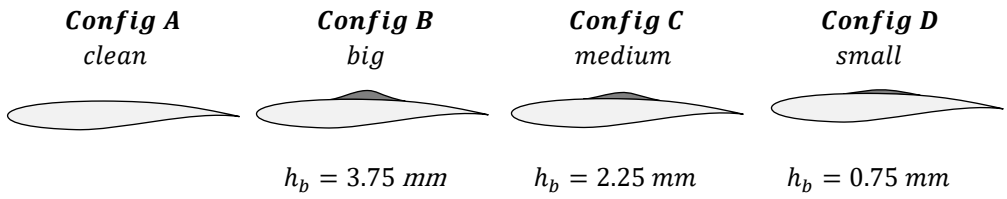

Figure 9: Configurations

3 RESULTS

The impact of bumps on the transonic dip is already evident from the preliminary results. By using bumps according to the configuration (see Figure 9), the Limit Cycle Oscillations (LCOs) or instabilities, the usual 'dip' pattern of the transonic dip seems to have disappeared in the ranges form 27 kPa to 70 kPa, as shown in Figure 10 (right). Instead, a 'wall' has emerged, essentially creating a 'Transonic Wall'.

Figure 10 (left) shows how the transonic dip is measured in the experiment for **Config A**. First, an initial pressure and a Mach number are set. Then, the oscillation behavior at the desired zero angle

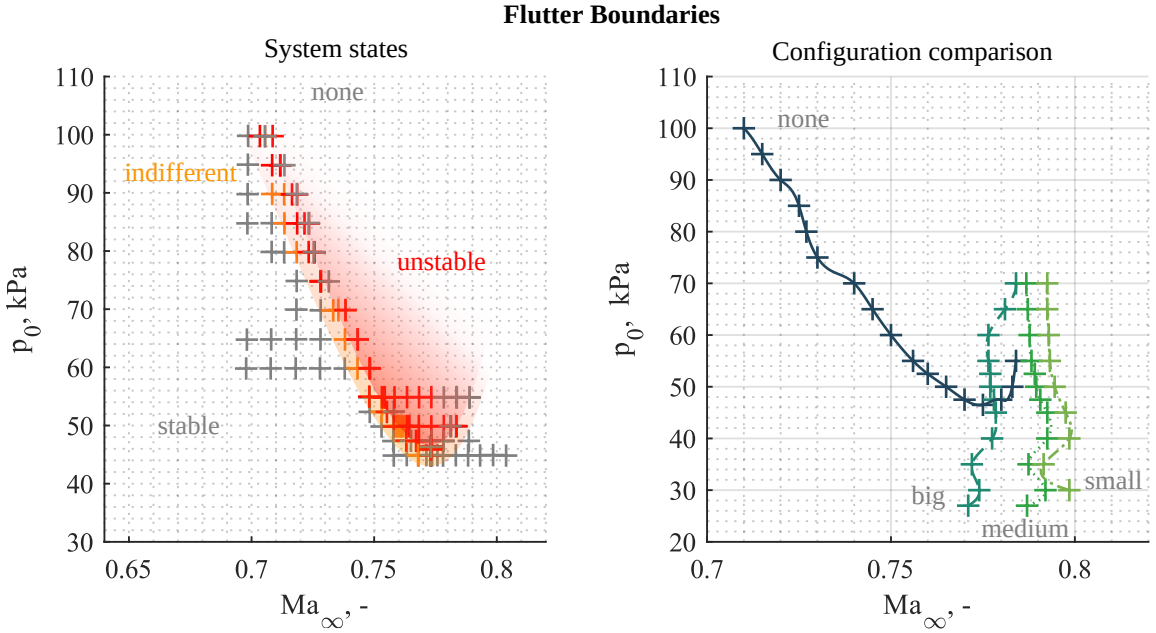

*Figure 10: **(left)** shows the system behavior for different pressures over the Mach-Number for Config A (none bump) at $\alpha_0 = 0°$, the beginning of the red area indicates the Flutter Boundary; **(right)** shows the Flatter Boundary for all configurations in comparison.*

of attack ($\alpha = 0°$) is recorded. If the system is stable or damped (stable), the Mach number is gradually and slowly increased until the system starts to enter a Limit Cycle Oscillation (LCO) or becomes unstable (unstable), if the system sometimes oscillates and dampens itself or the system is in a beat and is not clearly unstable or stable it is called (indifferent).

The procedure is repeated for each of the four configurations with different bump sizes. The flutter boundaries for all configurations are shown in Figure 10. The results show that the flutter boundary moves to higher Mach numbers for the smallest bump (**Config A**), while the largest bump (**Config B**) also increases the Mach numbers for flutter, but not as much as the other bumps.

The eigenfrequencies of the wing model are listed in Table 3. These values are obtained from a modal analysis, carried out before each measurement with wind. The first mode corresponds to the heave mode, while the third mode corresponds to the torsion or pitching mode.

	Mode 1 Hz	**Mode 2** Hz	**Mode 3** Hz	**Mode 4** Hz	**Mode 5** Hz	**Mode 6** Hz
Config A (none)	27,01	31,81	47,99	107,12	157,39	173,00
Config B (big)	26,86	31,81	47,76	106,81	156,86	172,88
Config C (medium)	27,01	31,74	47,76	107,73	157,62	173,03
Config D (small)	26,86	31,74	47,76	107,12	157,01	172,88

Table 3: Eigenfrequencies

Figure 11 provides a comprehensive view of the corresponding Power Spectral Density (PSD) of the ten accelerometers and the mode shapes. These elements are crucial in understanding the dynamic behavior of the system. Among the modes, Mode 1 is particularly significant as it represents the heave motion, denoted by (h). This motion is characterized by the vertical movement of the system. On the other hand, Mode 3 is associated with the torsional motion, represented by (α). This motion involves the twisting or rotational movement of the system. By studying these modes and the PSD, valuable insights can be gained into how the system responds to various internal and external forces.

The mode shapes display the amplitude and phase of each respective mode shape, normalized to the greatest deformation of each mode shape. The mode shapes have been interpolated and extrapolated from the accelerometer signals, as seen in Figure 7, onto the surface of the model.

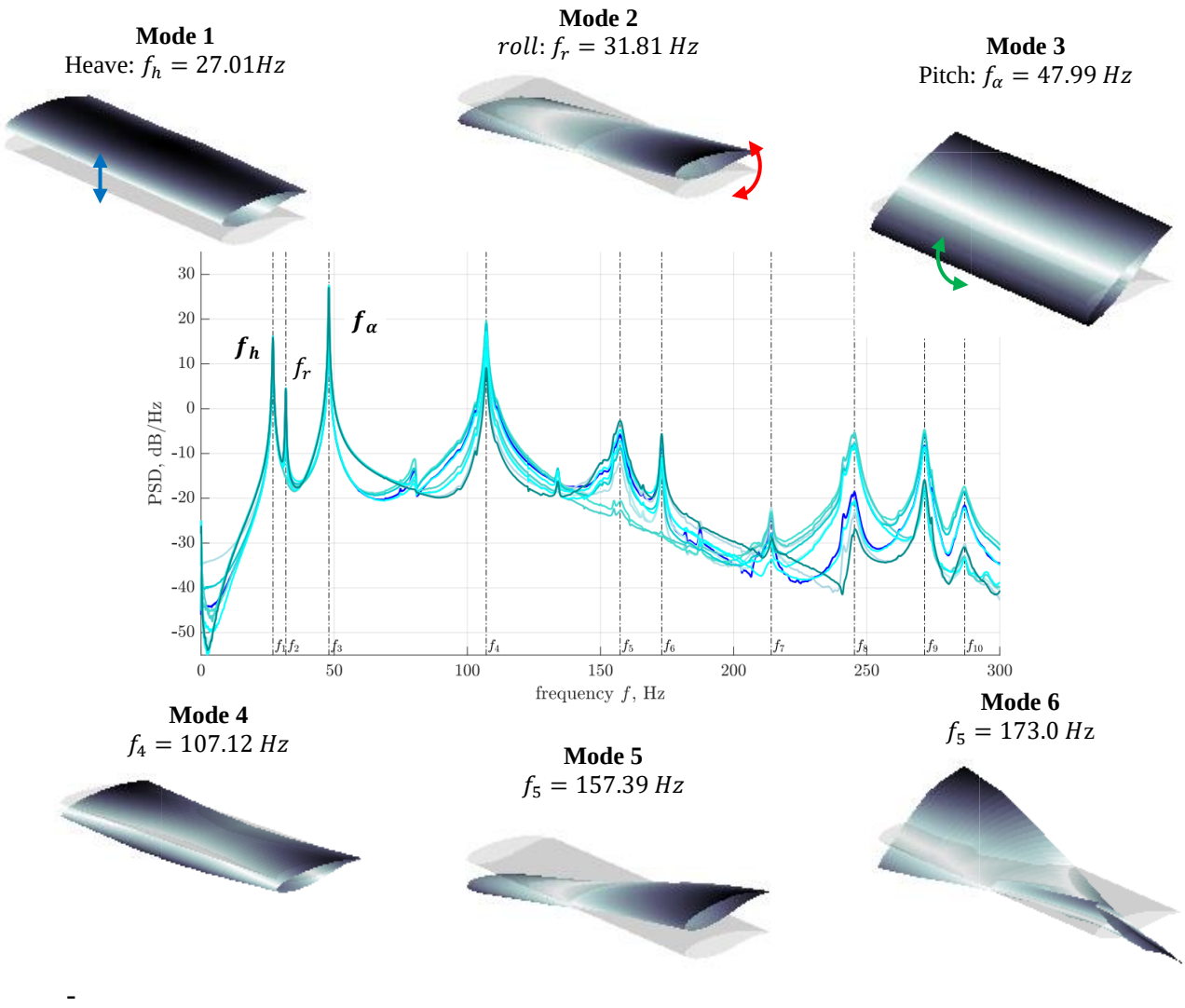

*Figure 11: Mode shapes and Modal analysis (via PSD) of **Config A** (before wind-test)*

Expanding on what is shown in Figure 10, Figure 12 presents the amplitudes of displacement (h) and torsion (α) along the flutter boundary. These values are determined from the acceleration signals originating from the center of the wingspan. The magnitudes of these amplitudes have been normalized to 1° for torsion and 1 mm for displacement. It is noticeable that in the configuration without a bump (**Config A**), heave is the dominant mode of oscillation. However, in configurations that include a bump, torsion becomes the first factor[1]. To provide a clearer picture, for each configuration, the signals of displacement and torsion are represented as time signals. These representations are given for the same static pressure $p_0 = 55\ kPa$.

In addition to showing oscillations (a), (b), (c), and (d), Figure 12 also presents a Power Spectral Density (PSD) analysis of the heave and alpha signals. This reveals how the main flutter mode varies. Building on this, Figure 14 displays the spectral analyses of all flutter cases against the pressure p_0. This highlights the impact that adding a bump has on the predominant flutter frequencies.

[1] It seems that the flutter in heave has disappeared, but the transonic dip shifted towards higher pressures. (see Outlook)

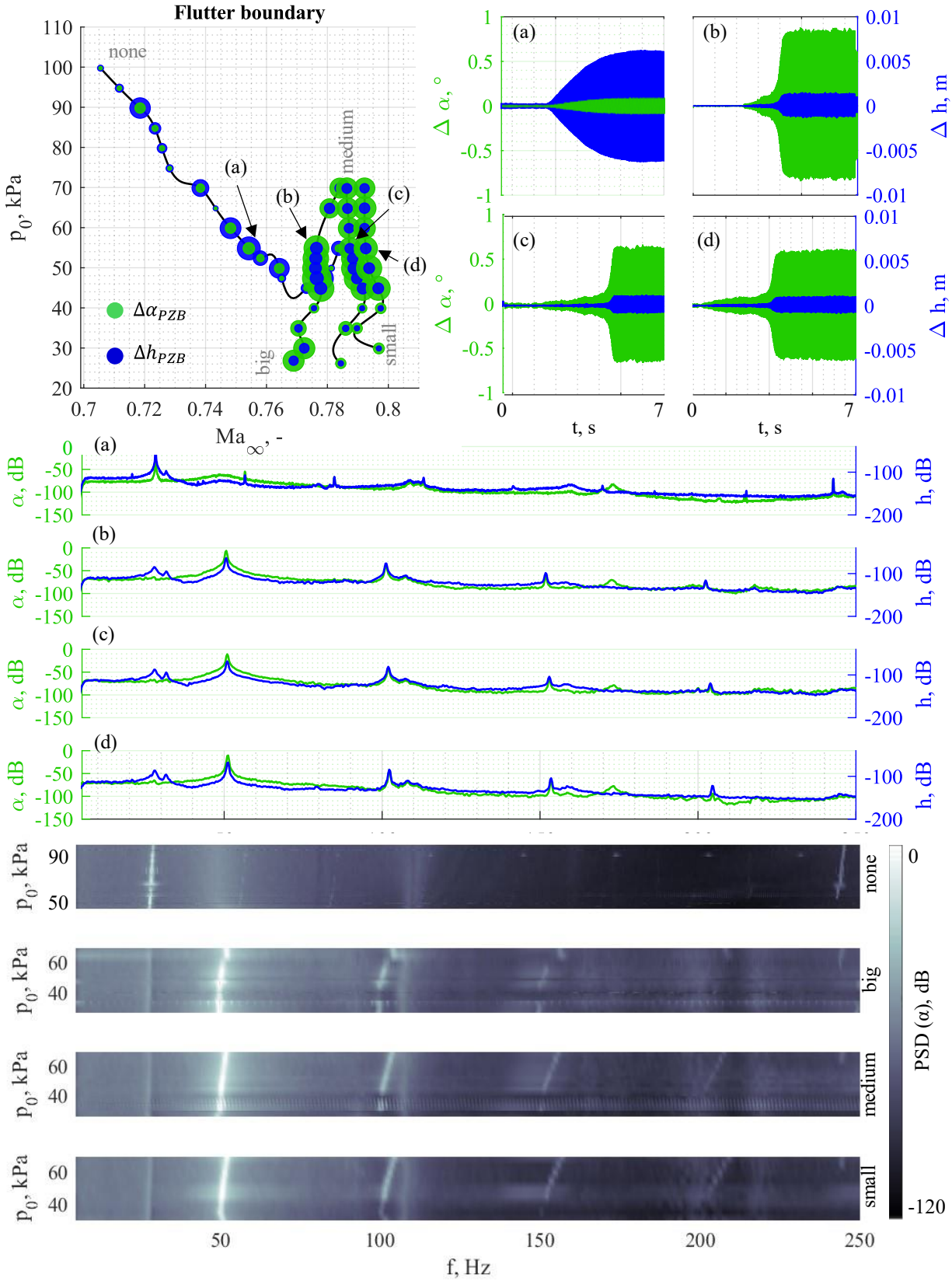

Figure 12: Flutter boundaries at $\alpha_0 = 0°$ with the corresponding amplitudes in heave (h) and torsion (α). Thereby heave and torsion are the two times integrated accelerometer signals of the both accelerometers located at b/2; in the figures middle the PSD of the heave and torsion signals is shown; the figures lower shows the PSD of the torsion over p_0

3.1.1 Pressure distribution and shock position

As depicted in the five upper plots in Figure 13, the pressure coefficients for **Config A** at 60 kPa are presented for various Mach numbers at a zero angle of attack. This representation provides a comprehensive view of how the pressure coefficients behave under different Mach numbers, which is crucial for understanding the aerodynamic performance of the airfoil. Interestingly, an increase

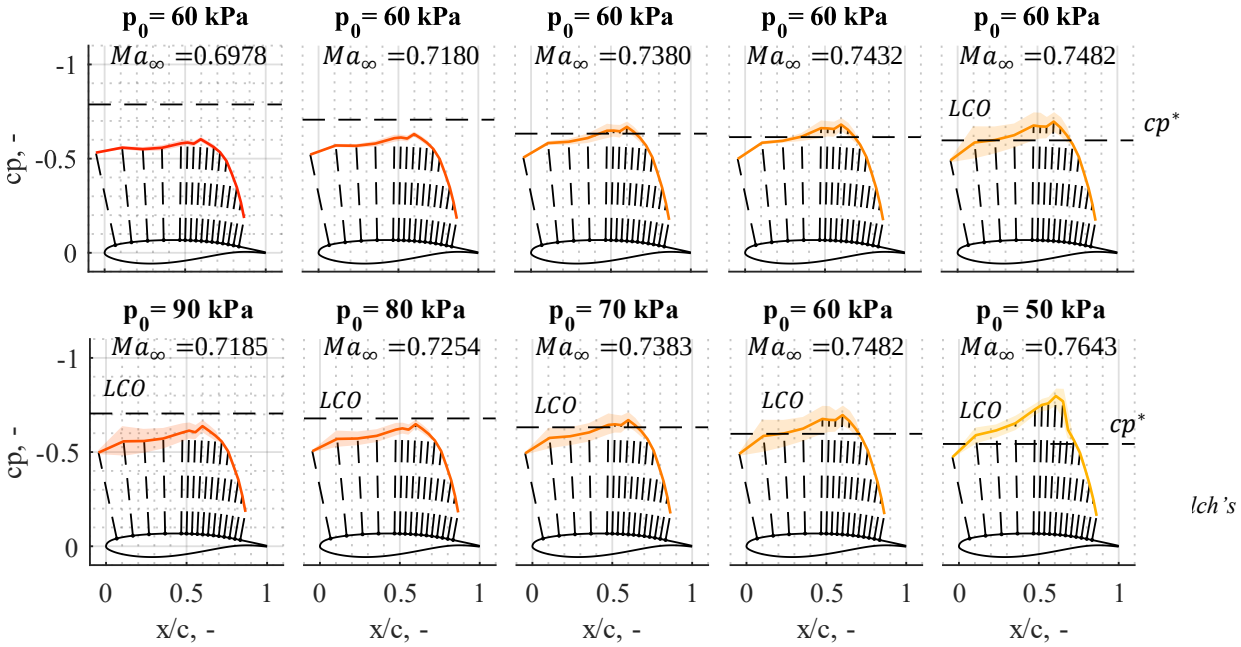

*Figure 13: Pressure distribution for different Mach-Numbers at same pressure (**upper**); along the flutter-boundary (**lower**)*

in the vibration amplitudes leads to a corresponding increase in the amplitudes of the pressure coefficient. This correlation suggests that the pressure distribution around the airfoil, and consequently its aerodynamic performance, can be influenced by controlling the vibration amplitudes. In addition to the previously discussed findings, the lower five plots in Figure 13 provides further insights by illustrating the pressure distributions of the LCO (Limit Cycle Oscillation) cases along the transonic dip. Finally, Figure 15 presents the temperature field of the model's upper side for the four cases (a), (b), (c), and (d) defined in Figure 12, as recorded by the infrared camera. Lower temperatures are indicative of a laminar flow, while higher temperatures correspond to a turbulent flow. It can be inferred that the application of Configurations B and C results in the shock being fixed by the bump.

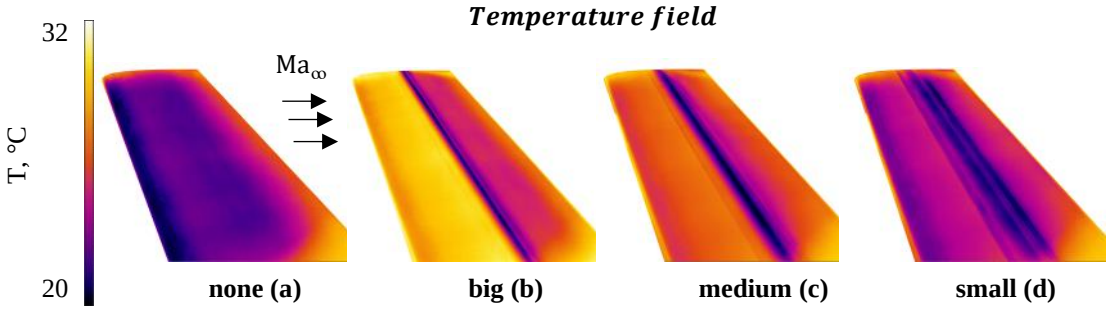

Figure 15: Temperature field of the model upper side recorded by the infrared camera at $p_0 = 55\ kPa$ and $\alpha_0 = 0°$

4 CONCLUSIONS

This study investigated the effects of three different bump configurations on the aeroelastic behavior of a typical section airfoil model in a transonic wind tunnel. The main findings are as follows:

- The bump height and position have a significant influence on the shock location, the pressure distribution, and the aeroelastic behavior.
- With increasing bump size, the shock-boundary layer interaction increases.
- As the bump size decreases, the "Transonic-Wall" shifts to higher Mach-Numbers.

5 OUTLOOK

The findings of this study offer valuable insights for the design and control of transonic airfoils with bumps. These insights can be leveraged to enhance the performance and stability of aircraft wings. However, further exploration is required to understand the impact of various parameters, such as the shape, size, and location of the bump, on the flutter characteristics. In addition, it is beneficial to gain a deeper understanding of the physics behind the flutter mechanism. To this end, it is advisable to detect shock movements. Measurements using the iPSP are already underway and the initial results are promising.

Figure 16, an extension of Figure 10, displays the flutter boundaries with Configuration D, but with iPSP film in orange. During the measurement, higher pressures were examined, which enabled the detection of the shift of the transonic dip in heave through the bump towards higher pressures.

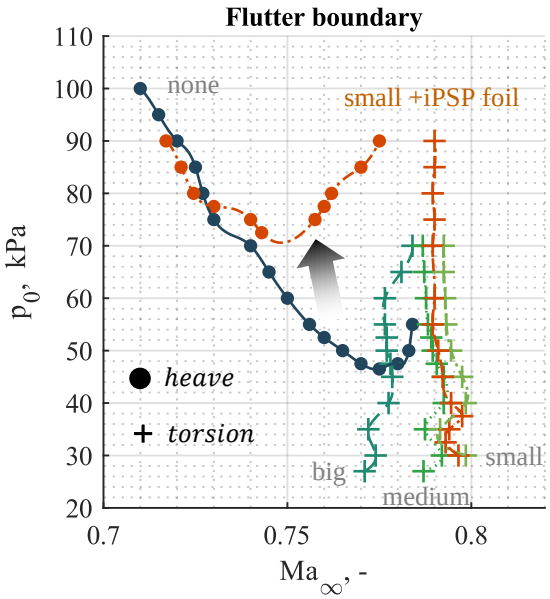

Figure 16: Outlook: Flutter boundary with small bump and iPSP at higher p_0

Furthermore, it would be intriguing to extend the analysis to three-dimensional models and compare the outcomes with those of two-dimensional models.

REFERENCES

[1] Tai, T.C., Huson, G.G., Hicks, R.M. and Gregorek, G.M, "Transonic characteristics of a humped airfoil," *AIAA*, vol. 87–1239 , 1987.

[2] Ashill, P.R., Fulker, J.L. and Shires, A, "A novel technique for controlling shock strength of laminar-flow aerofoil sections," *DGLR Bericht Part 6(92–01–022),* p. 175–183 , 1992.

[3] Z. Feng, "Flutter Phenomenon and Safety Implications in Transonic Flow," *AMCCE,* vol. 76, p. 7, 2023.

[4] P. Bruce and Colliss, S.P.;, "Review of research into shock control bumps," *Shock Waves,* vol. 25, p. 451–471, 2014.

[5] H. Hennings, J. Nitzsche, . J. Otte and C. Kaiser , "THE EFFECT OF SHOCK CONTROL BUMPS ON THE THE TRANSONIC FLUTTER AND BUFFETING CHARACTERISTICS OF A TYPICAL WING SECTION," *IFASD,* 2022.

[6] W. Wadehn, A. Sommerer, Th. Lutz, D. Fokin, and G. Pritschow, S., "STRUCTURAL CONCEPTS AND AERODYNAMIC DESIGN OF SHOCK CONTROL BUMPS," *ICAS,* 2002.

[7] A. Goerttler, S. Künnecke and C. Sabater, "Aerodynamic Design of Shock Control Bumps Considering Structural Constraints," *STAB/DGLR Symposium 2022,* vol. New Results in Numerical and Experimental Fluid Mechanics XIV, p. 671–681, 2023.

[8] M. Kintscher, J. Riemenschneider and H. Monner, "Structural concept of an adaptive shock control bump spoiler," *CEAS Aeronautical Journal,* vol. 12, no. https://doi.org/10.1007/s13272-021-00507-9, p. 509–518, 2021.

[9] M. Kintscher, Nuno Alves de Sousa, . H. P. Monner and M. Wiedemann, "Generation of a Shock Control Bump by Pressurized Chambers," *ICAST - 26th International Conference on Adaptive Structures and Technologies,* 2015.

[10] W. Haase, B. Aupoix, U. Bunge and D. Schwamborn, "OAT15A airfoil in wind tunnel (Alenia, Dassault)," *FLOMANIA — A European Initiative on Flow Physics Modelling,* p. 225–232, 2006.

[11] A. D'Aguanno, F. Schrijer and van Oudheusden, "Experimental investigation of the transonic buffet cycle on a supercritical airfoil," *Exp Fluids,* vol. 62, 2021.

[12] A. Accorinti, et and al, "Measurements of deformation, schlieren and forces on an OAT15A airfoil at pre-buffet and buffet conditions," *10th EASN,* vol. IOP Conf. Ser.: Mater. Sci. Eng. 1024 012052, 2020.

[13] M. Braune, Identification of a flutter mechanism on a supercritical airfoil with laminar flow, http://dx.doi.org/10.53846/goediss-8675, 2021.

COPYRIGHT STATEMENT